Computational Assessment of the Impact of Wave Count on Rotating Detonation Engine Performance

Daniel E. Paxson[1]
NASA Glenn Research Center, Cleveland, Ohio, 44130

The impact of the number of azimuthally propagating waves on the performance of a Rotating Detonation Engine (RDE) is investigated using a simplified two-dimensional computational fluid dynamic simulation. The basic RDE configuration examined has no exit throat. The inlet is assumed lossless and does not allow backflow. The adiabatic, inviscid, and premixed simulation utilizes a particularly simple finite rate reaction mechanism that allows user control over the relative amounts of deflagration and detonation that occur, the presence and extent of a reaction delay associated with fuel and oxidizer mixing, and the number of waves present in the domain. The simplifications and idealizations decouple the effect of wave count from other potential loss mechanisms. Performance is measured using exhaust flow total pressure gain relative to the inlet total pressure. One, two, and three wave solutions are computed under identical boundary conditions and grid resolution. For simulations with no mixing delay and minimal deflagration, the number of waves present has negligible impact on performance. With a mixing delay, performance decreases with increasing wave number. With increased deflagration, performance increases with increasing wave number. With both effects simulated it is found that the two wave solution performs better than either the one or three wave solutions. The causes of these trends are explored. They imply that for practical, RDE's, the number of waves that are present can impact performance.

Nomenclature

a	=	non-dimensional speed of sound
D_m	=	mean diameter
D_T	=	thermal diffusion coefficient
D_z	=	species diffusion coefficient
EAP_i	=	ideal Equivalent Available Pressure
$\underline{F}$	=	azimuthal flux vector
$\underline{G}$	=	axial flux vector
h	=	annular channel height
K_0	=	non-dimensional reaction rate constant
l	=	mean circumference
mfr	=	non-dimensional mass flow rate
P	=	total pressure
p	=	non-dimensional pressure
PG	=	Pressure Gain
q_0	=	non-dimensional heat addition parameter
$\underline{S}$	=	source term vector
t	=	non-dimensional temperature
T	=	non-dimensional temperature

[1] Aerospace Research Engineer, Research and Engineering Directorate, 21000 Brookpark Road/MS 77-1, AIAA Associate Fellow

T_{c0} = non-dimensional threshold temperature
u = non-dimensional azimuthal velocity
v = non-dimensional axial velocity
$\underline{w}$ = conserved variables vector
x = non-dimensional azimuthal distance
y = non-dimensional axial distance
z = reactant mass fraction

Greek
γ = ratio of specific heats
ρ = non-dimensional density

Subscripts
a = ambient
det = detonation
m = inlet manifold
max = maximum

Superscripts
$*$ = reference value

I. Introduction

Rotating Detonation Engines (RDE's) generally operate with 1-4 dominant detonation waves propagating around the annular combustor simultaneously. When there is more than one wave present, modes of operation can occur where all of them travel in the same direction or where they travel in opposing directions. There is little consensus in the community as to what determines the number of waves or their direction. Experimental RDE's can even exhibit different numbers of waves and wave directions at different times during a single run. To date, no experiment has been published showing a capability to control or determine ahead of time the wave count or mode that will be present under a given set of operating conditions (though most experiments are consistently able to repeat the count and mode from run to run). More importantly, there is little information about the impact that wave count has on RDE performance. This is partly because RDE's are highly coupled devices, and it is difficult to isolate the performance effects of one phenomenon from another. It may also be partly because RDE technology has not yet developed to the point where pressure gain has been demonstrated [1]. This means that the performance impact of wave count, if it is of a secondary nature, may be masked by more primary impacts such as backpropagation and forward flow losses associated with RDE inlets [2].

The present work seeks to assess the performance impact of detonation wave count using a simplified computational fluid dynamic (CFD) simulation of an idealized RDE [3]. The use of simplification and idealization provides a kind of decoupling of the effect of wave count from other potential loss mechanisms, and it resolves the masking issue just discussed. It also allows the specification of wave count since detonations can be directly initiated anywhere in a simple computing domain.

The fully ideal RDE is first described, followed by a brief description of the simulation. Preliminary results are then presented whereby a single operating point is simulated with either 1, 2, or 3 co-rotating waves present. It is demonstrated that for the fully idealized RDE, the wave count has negligible effect on performance as measured by Ideal Equivalent Available Pressure, EAP_i [4]. Ideal Equivalent Available Pressure is a single pressure representing the maximum work availability of the spatially and temporally non-uniform exhaust flow. It is defined as the total pressure which, when isentropically expanded to the ambient pressure at the mass flux averaged total enthalpy of the RDE exhaust, produces the computed ideal specific thrust. Ideal specific thrust is computed using the ideal specific thrust of each fluid element in the exhaust exit plane and then mass flux averaging the result.

A simple sub-model is then added to approximate what are often called mixing delays observed in most experimental RDE's. With this sub-model in place, it is found that the more waves that are present, the more EAP_i is reduced. A sub-model for another experimentally observed phenomenon, deflagrative pre-burning is also examined. Here it is found that the more waves that are present, the less EAP_i is reduced. Simulations are also examined where the two phenomena are combined. These show that peak performance is obtained with 2 waves; however, this performance is well below that of the fully idealized RDE.

II. Simulation Setup

A. RDE Description and Operating Conditions

Shown schematically in Fig. 1, the particular RDE simulated has a mean diameter, D_m of 5.5 in. The axial length is 5.2 in. The annular channel height, h is uniform along the entire axial length. The flow is assumed inviscid and adiabatic. As such, the channel height is irrelevant other than to stipulate that it is small in comparison to D_m. This validates the two-dimensional (2D) assumption of the CFD simulation described below.

The operating conditions for the RDE are a manifold total temperature of T_m=540 R, a manifold total pressure of P_m=58.8 psia, and exits to an ambient static pressure of p_a=14.7 psia. The working fluid is premixed hydrogen and air at an equivalence ratio of 1.0.

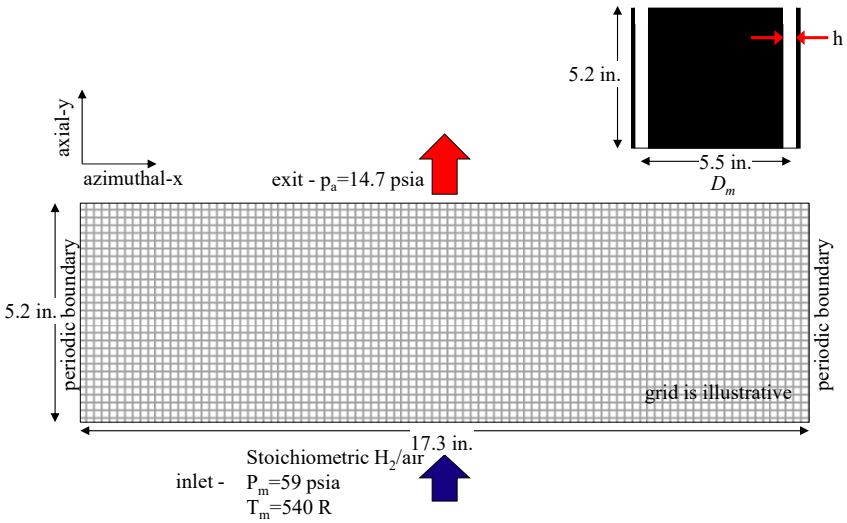

Fig. 1 RDE Schematic and associated computational domain

B. Simulation Description

Details of the CFD simulation are described in Refs. [3, 5]. Governing equations, numerical integration approach and boundary conditions specifically used in the present work are briefly described below.

1. *Governing Equations and Non-Dimensionalization*

On the assumptions that the annulus radius of curvature is much greater than its height, and that the working fluid is a single calorically perfect gas, the governing equations of motion are written in non-dimensional, detonation frame of reference form as follows.

$$\frac{\partial \underline{w}}{\partial t} + \frac{\partial \underline{F}}{\partial x} + \frac{\partial \underline{G}}{\partial y} = \underline{S} \tag{1}$$

where

$$\underline{w} = \begin{bmatrix} \rho h \\ \rho u h \\ \rho v h \\ \left(\frac{p}{\gamma(\gamma-1)} + \frac{\rho(u^2+v^2)}{2} + \rho z q_0\right) h \\ \rho z h \end{bmatrix} \tag{2}$$

$$\underline{F} = \begin{bmatrix} \rho u h \\ \left(\frac{p}{\gamma} + \rho u^2\right) h \\ \rho u v h \\ u\left(\frac{p}{(\gamma-1)} + \frac{\rho(u^2+v^2)}{2} + \rho z q_0\right) h \\ \rho u Z h \end{bmatrix} \tag{3}$$

$$\underline{G} = \begin{bmatrix} \rho v h \\ \rho u v h \\ \left(\frac{p}{\gamma} + \rho v^2\right) h \\ v\left(\frac{p}{(\gamma-1)} + \frac{\rho(u^2+v^2)}{2} + \rho z q_0\right) h \\ \rho v z h \end{bmatrix} \tag{4}$$

$$\underline{S} = \begin{bmatrix} 0 \\ 0 \\ \frac{p}{\gamma}\frac{dh}{dy} \\ 0 \\ -\rho z \begin{Bmatrix} K_0; T \geq T_{c0} \\ 0; T < T_{c0} \end{Bmatrix} h \end{bmatrix} \tag{5}$$

The governing equations are closed with the non-dimensional equation of state, which is written as follows.

$$p = \rho T \tag{6}$$

Non-dimensionalization of pressure, density, temperature, and velocity components is obtained using reference values p^*, ρ^*, T^*, and the corresponding sound speed, a^*. The x (azimuthal) and y (axial) distances are non-dimensionalized using the mean circumference, l. The time is non-dimensionalized using the acoustic wave transit time, l/a^*. The non-dimensional annulus height (often called the channel width), h is referenced to the physical annulus height at the inlet end of the RDE. Since the configuration studied here has a uniform annulus height, h=1.0 at every axial location. The source term vector, Eq. 5 normally contains expressions to account for wall friction, area variation, wall heat transfer, and reaction rate. Since the present analysis is adiabatic and inviscid, only the reaction rate and area variation terms are non-zero. However, the latter of these two is also zero because dh/dy=0.0. With the non-dimensionalization process now described, unless otherwise stated, all variables discussed are non-dimensional.

The global finite rate reaction model defined in Eq. 5 is a simplification governed by the reactant mass fraction, z, the density ρ, a rate constant, K_0, and a threshold temperature, T_{c0}. K_0 replaces the typical Arrhenius-type reaction rate with a step-function. The heat of reaction of the reactant gas mixture, q_0 depends on the fuel heating value, the air-to-fuel ratio of the premixture, and the reference speed of sound.

Relevant parameters for the present simulation are listed in Table 1. In order to delineate between regions of detonation and deflagration, a pressure threshold is also applied to the reaction rate constant when $T>T_{c0}$.

$$K_0 = \begin{Bmatrix} 280; p \geq 4.0 \\ 12; p < 4.0 \end{Bmatrix} \tag{7}$$

2. *Numerical Treatment*

The governing equations are integrated numerically in time using an explicit, second-order, two-step, Runge-Kutta technique. Spatial flux derivatives are approximated as flux differences, with the fluxes at the discrete cell faces evaluated using Roe's approximate Riemann solver. Second-order spatial accuracy (away from discontinuities) is obtained using piecewise linear representations of the primitive variable states within the cells (aka, Monotonic Upstream-centered Scheme for Conservation Laws or MUSCL). Oscillatory behavior is avoided by limiting the linear slopes.

Table 1 Simulation Parameters

γ	1.264
q_0	23.4
p^*, psia	14.7
T^*, R	520
a^*, ft/s	1250
ρ^*, lb_m/ft^3	0.055
T_{c0}	3.5

3. *Boundary Conditions*

Considering an 'unwrapped' RDE (Fig. 1), the following boundary conditions are imposed. At x=0.0 and x=1.0, periodic conditions are used. This means the rightmost boundary image cells are assigned the value of the leftmost interior cells at each y location. Similarly, the leftmost boundary image cells are assigned the value of the rightmost interior cells. The periodic boundary ensures that the azimuthal dimension of the computational space faithfully

represents an annulus (which is continuous and has no actual boundary). At the exit plane, $y=y_{max}$, constant ambient pressure outflow is used along with characteristic equations to obtain ρ, and v for the image cells. If the resulting flow is sonic, or supersonic, then the imposed pressure is disregarded. If, in addition, the upstream flow is supersonic, then p, ρ, and v are extrapolated from the interior. The possibility for a normal shock solution whereby supersonic outflow jumps to subsonic is also accommodated. The azimuthal velocity component, u, is set equal to the last interior cell at each x location in the plane.

At y=0.0 (the inflow face), fully open boundary conditions are applied as described in Ref. [3]. This face is presumably fed by a large manifold at a fixed total pressure, P_m, and total temperature, T_m. The manifold terminates at the face and is separated from it via a perfect valve. If the interior pressure is less than P_m then isentropic inflow occurs. The boundary condition routine determines p, ρ, and v for the inflow face image cells such that the characteristic equations are satisfied between it and the first interior cell (at the same x position), while maintaining isotropy with the manifold. The azimuthal velocity component is prescribed during inflow, and it is here that a reference frame change is implemented. Rather than specify u=0 (i.e., no swirl), the negative of the detonation speed, u_{det}, is prescribed instead. As a result of this change to the detonation reference frame, the computational space becomes one where a steady-state solution is possible. If the interior pressure along the inlet face is greater than P_m, as might be found just behind the detonation, a slip wall boundary condition is applied (i.e., no flow normal to the face is allowed). This is also sometimes referred to as a symmetry boundary condition.

4. *Solution Procedure*

The prescribed detonation speed is not known a priori. It must be found iteratively. An initial guess is made for u_{det} and the simulation is run for the amount of time corresponding to approximately three annular revolutions of the detonation. The domain is then examined to determine if the detonation has migrated from its initial position. If it has moved to the right of where it started, then the initial guess at u_{det} is too high. If the detonation front has moved to the left, then the initial guess is too low. Based on these results, a new guess is made for u_{det}, and the simulation is run for another 3 cycles. The process continues until the detonation front remains stationary and the entire domain becomes temporally stationary. As described in [3], a course grid is used deliberately. For the present simulation only 108,000 uniformly spaced grid points define the domain (600×180).

The process of initializing the simulation such that the flow field contains a detonation on which speed iterations can be made is outlined in Ref. [3]. The number of waves present in the annulus are prescribed by the user when the simulation is initialized. The course grid and simplified reaction mechanism of the simulation preclude the spontaneous formation of additional waves or extinction of initialized waves.

III. Results

A. Ideal Solutions

Converged flowfield solutions to Eq.1 are shown in Fig. 2 for one, two, and three wave simulations. Solutions are represented by contours of temperature. Also shown in each contour is a dashed black line representing the region where the detonative reaction occurs. Inside this region the temperature is above T_{co} and z is above 0.1.

This is where all the pressure gain occurs. As the flow exits this region (in the detonation frame of reference) its total pressure drops. This is partly due to losses inherent to the RDE cycle, but mostly due to the necessity that, for all fundamentally unsteady constant volume cycles, work must be done to get fluid out of the control volume [6]. The EAP_i measurement used to assess performance takes this drop into account because it is measured in the exit plane (i.e., y=0.3). Each contour in Fig. 2 lists the associated pressure gain, PG, azimuthal detonation wave propagation speed, u_{det}, and mass flow rate, mfr. PG is expressed as a percentage and defined as follows.

$$PG = \left(\frac{EAP_i}{P_m} - 1\right) \times 100 \tag{8}$$

The wave speed is written as a percentage of the theoretical Chapman-Jouguet detonation speed for a one-dimensional wave. It shown in Fig. 1 that PG and mfr are largely independent of the wave number (other than a slight decrease in PG in the 3-wave solution). However, wave speed decreases with increasing wave number. A possible reason for this speed decrease is discussed in Ref. [7] and briefly summarized as follows. Consider Fig. 3 which shows an exploded view of the Fig. 2 reaction regions for the 1 and 3-wave solutions. Though seemingly narrow in its azimuthal extent, this is actually quite a wide reaction zone when compared to other ideal, 2D, CFD RDE solutions [8]. It is an artifact of the course grid and simplified reaction mechanism used here. However, as discussed in Ref. [7] a number of small length-scale, large amplitude non-uniformities in real-world RDE flowfields (e.g. intense turbulence,

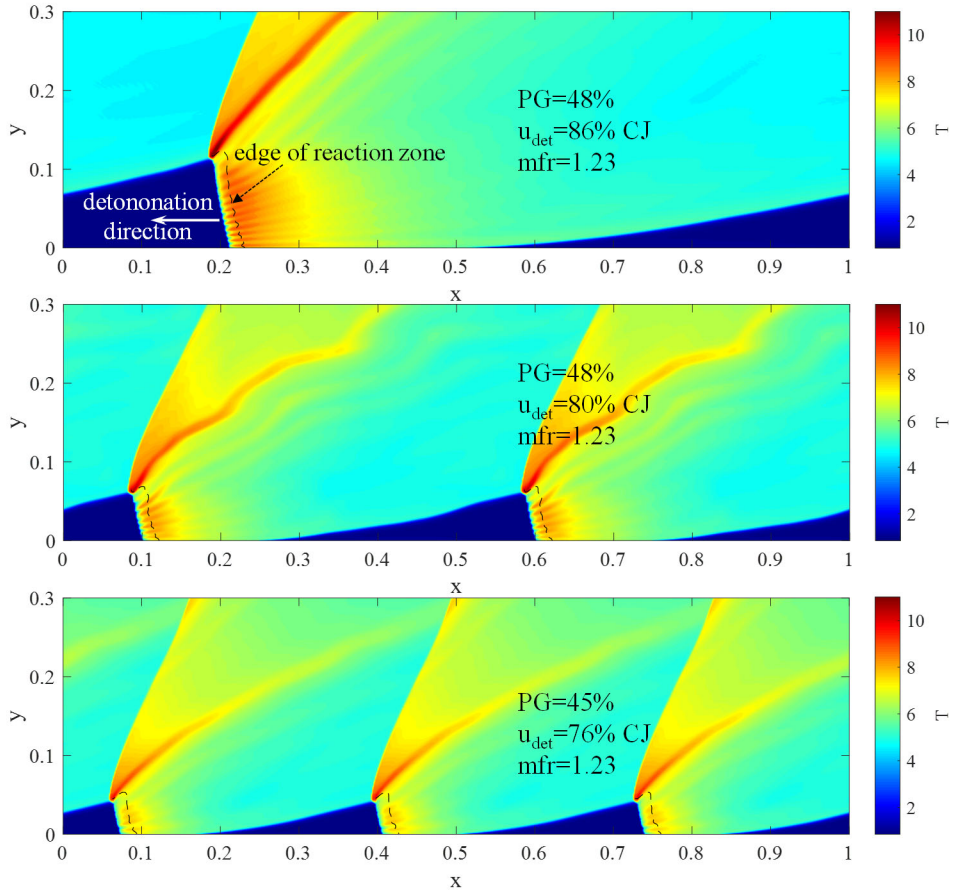

Fig. 2 Contours of temperature for the 1-wave (upper), 2-wave (center), and 3-wave (lower) solution to the ideal RDE flowfield

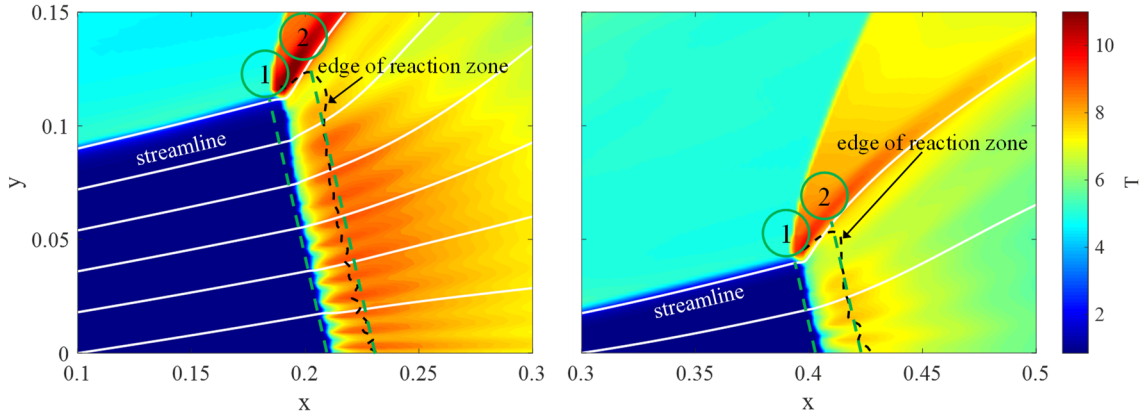

Fig. 3 Contours of temperature in the reacting region for the (a) 1-wave, (b) 3-wave solution to the ideal RDE flowfield

incomplete fuel and air mixing, baroclinic forces, etc.) could give rise to relatively wide reaction zones. It is evident in both Fig. 3a and 3b that fluid streamlines are diverging in the reaction zone. This implies fluid expansion during heat addition. This in turn implies reduced confinement of the reacting fluid when compared to a strictly one-dimensional detonation reaction zone. Reduced confinement leads to reduced pressure to drive the coupled shock wave. Shock propagation speed, which is the same as u_{det}, is directly related to shock pressure ratio. Thus, the more

divergent the streamlines of Fig. 3, the lower the value of u_{det}. This process is sometimes referred to as lateral relief [9] since it arises from one side of the reaction zone being unbounded (when compared to a one-dimensional detonation in a tube where both sides of the reaction zone are bounded by walls). The lengths of the dashed green lines in Fig. 3 labeled 1 and 2 can be used as a crude measure of reaction zone divergence. Specifically, the difference between lengths 2 and 1 is the measure of interest. It is seen that this difference is similar in Fig. 3a and 3b. However, Fig. 3b is processing only a third of the flow passing through the RDE (there are 3 detonations present in the annulus). The divergence per unit of mass flow is therefore 3 times greater for the 3-wave solution than for the 1-wave solution. Though not shown, it follows from this argument that the 2-wave solution would have divergence per unit of mass that is intermediate between the 1 and 3 wave solutions. Since more divergence leads to lower detonation speeds, the trend shown in the listed u_{det} values of Fig. 2 is expected. It is interesting to note that this trend is consistent with experimental results [10]. Note too that in this idealized scenario, reduced detonation speed does not strongly correlate with reduced performance. Possible reasons for this are discussed in Ref. [7].

B. Impact of Mixing Delay

It has been noted experimentally [11, 12] that the detonation wave often propagates around the RDE annulus at a small axial distance downstream of the head end (i.e., downstream of the inlet trailing edge). The cause of this so-called stand-off distance is likely related to the fact that RDE's are not operated in a premixed fashion. Instead, fuel is injected into the incoming airflow stream and generally takes some time, or axial convective distance, to mix before it will detonate. In order to study the impact of this mixing delay, the present simulation was modified such that the Eq. 5 reaction rate constant, K_0, was set to 0.0 even if the fluid temperature exceeded T_{c0} for all values of $y \leq 0.015$. This is approximately 5% of the axial length. It is longer than is typically observed experimentally. And the assumption that there is no reaction whatsoever in the delay region is likely an oversimplification. However, these parameter value choices do clearly illustrate the mixing delay effect. These are shown in Fig. 4 in a similar fashion to Fig. 2. The mixing delay, with location denoted by a dashed white horizontal line, creates a flow field with an oblique shock running upstream toward the inlet. The oblique shock is generated by the detonation wave which is essentially 'pushing' the incoming air back upstream temporarily and compressing it. In order to show the oblique shock clearly, pressure contours in the vicinity of the detonation are shown in Fig. 5 for the 2-wave solution.

Returning to Fig. 4, this shock is found to be dissipative in that the associated compression does not ultimately produce useful work. The predominant effect is to heat (i.e. add entropy to) a portion of the incoming flow prior to detonation.

The heated flow is then processed by the next detonation, ultimately producing less pressure rise across it and lower overall pressure gain. The pressure gain values listed in Fig. 4 are lower than those of Fig. 2. The streamlines shown in Fig. 4 illustrate the process. The white streamline represents the outer bound of reactant that enters the RDE from the manifold, is heated as it passes through the upstream propagating shock, and finally passes through the downstream portion of the subsequent detonation. The yellow streamline represents the outer bound of reactant that enters the RDE from the manifold and travels directly through the detonation. Figure 6 shows total temperature versus entropy along two streamlines of the 1-wave solution to illustrate the processes described. The black curve represents a streamline originating at x=0.825, y=0. It does not pass through the upstream running oblique wave. The red curve represents a streamline originating at x=0.175, y=0. It does encounter the oblique. The additional entropy generated by the oblique wave is evident. The total pressure on the black line at the point where the reaction completes is nearly twice that of the corresponding point on the red line.

The mixing delay is assumed to be the same axial length regardless of the number of waves present. As such, Fig. 4 illustrates that as the number of waves increase, the fraction of incoming reactant that is heated by the upstream running oblique shock increases. Consequently, as the wave count goes up the pressure gain goes down. Since the shock heating makes the incoming reactant less dense, it follows that mixing delay reduces mass flow rate relative to the fully idealized scenario of Fig. 2. To illustrate this in the detonation frame of reference, consider the dashed green lines marked with the circled number 1 in the 1-wave contours of Figs. 3 and 2. The average normal mass flux rate across these lines, multiplied by their lengths closely approximates the RDE mass flow rate. The average mass flux rate can be approximated by the product of u_{det} and the average density along the dashed line. For the Fig. 4 line, this density is 87% of the corresponding Fig. 3 density (due to the shock heating). The Fig. 4 dashed line is 12.5% longer than that of Fig. 3. The value of u_{det} for Fig. 4 is 99% of the value for Fig. 3. Thus, the mass flow rate of the Fig. 4, 1-wave solution is estimated to be $1.125 \times 0.87 \times 0.99 = 0.97$ that of the Fig. 3, 1-wave solution, which it is. This brief analysis demonstrates that for any of the flowfield temperature contours shown, the warmer the entering fluid becomes prior to encountering the detonation, the lower the mass flow rate. For the mixing delay solutions as the wave count goes up, a larger fraction of the flow is shock heated, so the mass flow rate goes down.

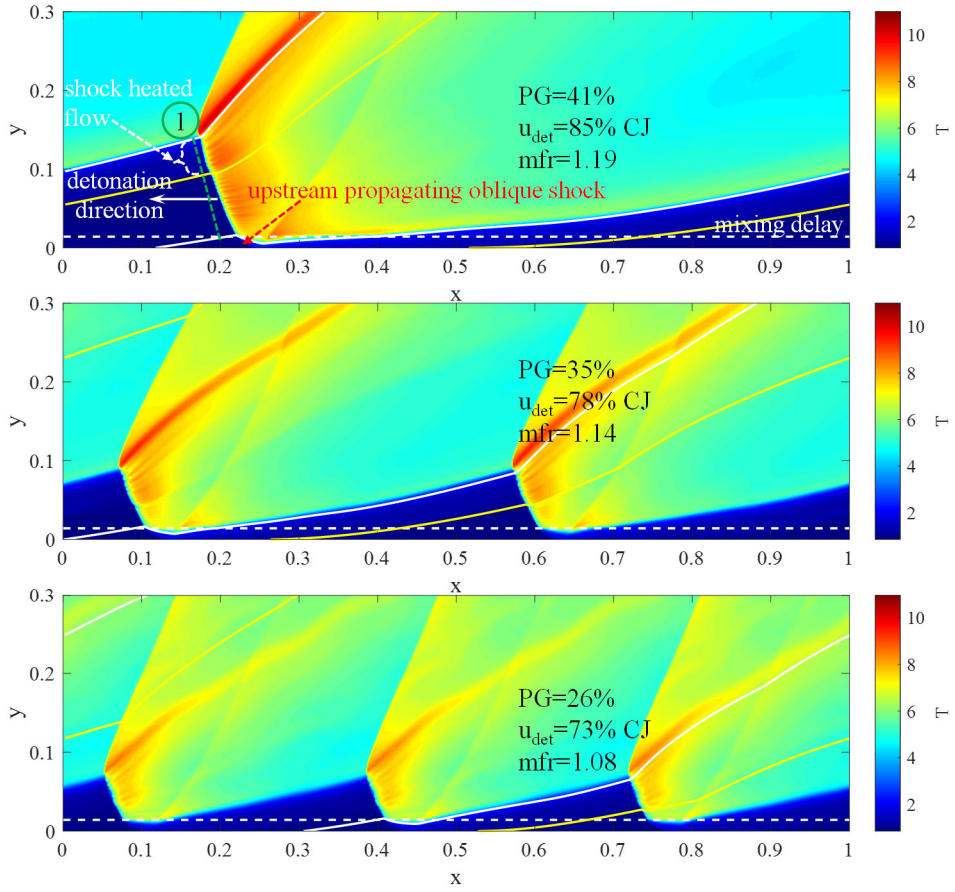

Fig. 4 Contours of temperature for the 1-wave (upper), 2-wave (center), and 3-wave (lower) solution to the RDE flowfield with mixing delay

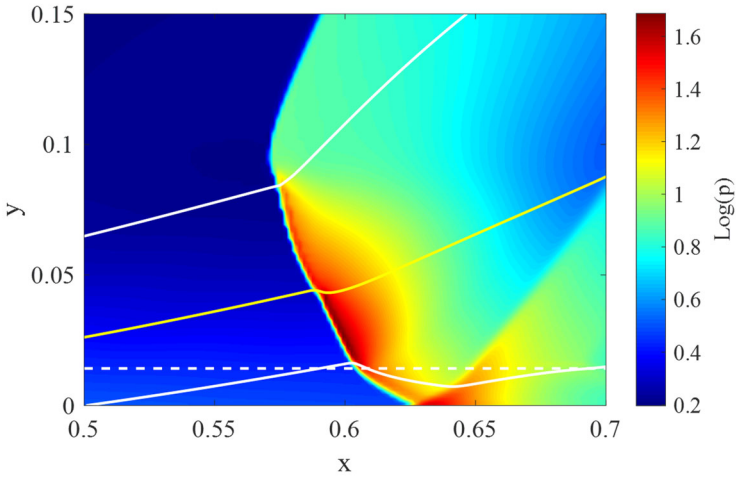

Fig. 5 Contours of Log(pressure) near the reacting region for the 2-wave solution to the RDE flowfield with mixing delay

The wave speeds are only slightly affected by the mixing delay and so follow the same trend as Fig. 2. That each wave speed listed is slightly less than its Fig. 2 counterpart is likely due to the observation that the mixing delay adds a small degree of so-called lateral relief in the upstream direction and therefore magnifies the effect discussed in the previous sub-section.

C. Impact of Deflagrative Pre-Burning

Because RDE inlets generally have some type of geometric flow restriction followed by a near step change in cross section, there are necessarily regions in the annulus where hot, post-detonation gases are trapped and/or recirculating. These can in turn ignite portions of the incoming fuel and air mixture (even if they are not fully mixed) [13]. The result is a sort of partial flame holding process whereby some of the incoming chemical energy is lost to deflagrative heat release during the fill process rather than being released in the detonation reaction zone. It will be referred to as pre-burning in this work. In order to explore this highly three-dimensional phenomenon in the context of the current simulation, the reaction

rate constant in Eq. 5 was modified as follows. In regions where the $T<T_{c0}$ the reaction rate was changed from 0.0 to K_0=2.0. This is just 0.7% of the detonative value, thus assuring that the reaction proceeds slowly in this region. Such a simple model has proven effective at interpreting results from experimental RDE's with backward facing steps at the inlet exit plane [14]. The results for the 1, 2, and 3-wave solutions are shown in Fig. 7 in similar fashion to Fig. 2. The effect of the pre-burning is evident in the temperature contours; particularly in the 1-wave solution. Here the incoming premixture is at an elevated temperature (i.e., a lighter shade of blue) directly ahead of the detonation wave when compared to the temperature at the same location in Fig. 2. This location is shown as a dashed green line in the upper contour of Fig. 7. In the detonation frame of reference this line can be thought of as a plane across which the reactant flows before passing through the detonation. To highlight the changing temperature of the inlet flow, contour lines representing T=1.5 and 2.0 are shown as dashed red lines. Also shown in yellow is a representative

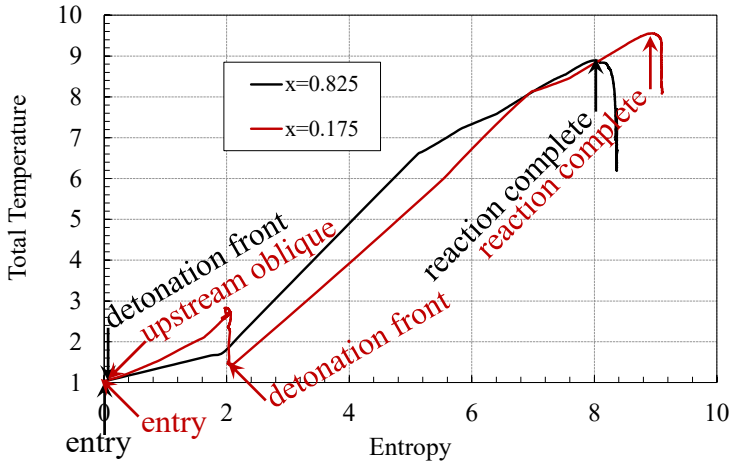

Fig. 6 Total temperature vs entropy along two streamlines of the one-wave solution

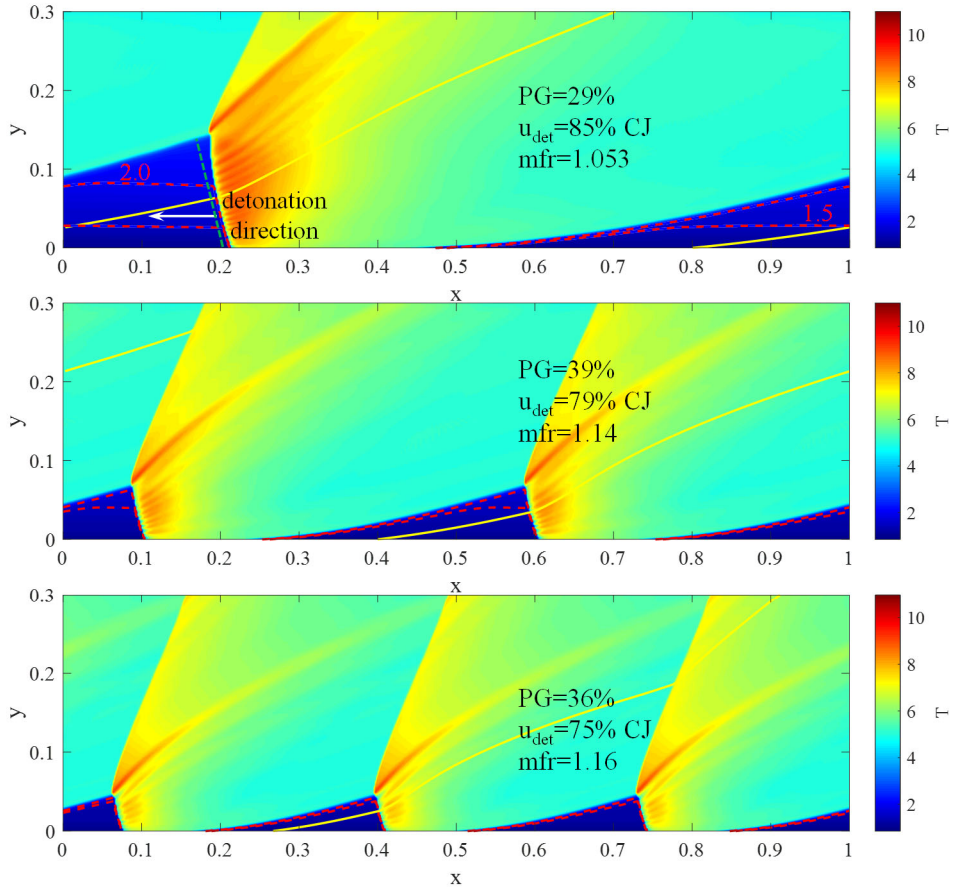

Fig. 7 Contours of temperature for the 1-wave (upper), 2-wave (center), and 3-wave (lower) solution to the RDE flowfield with deflagrative pre-burning

inflow streamline. Following this streamline from left to right in the figure clearly demonstrates the heating that occurs due to the low-level reaction taking place as a fluid element moves through the fill zone. The mass flux averaged reactant fraction along the dashed green line is 0.85 for the 1-wave solution, 0.89 for the 2-wave solution, and 0.93 for the 3-wave solution. This indicates that more of the reactant is consumed via pre-burning as the wave count goes down. This makes sense since the time available for pre-burning goes up as wave height (i.e., axial extent of the detonation front) goes up, and the wave height goes up as the wave count goes down.

Reactant consumed in pre-burning does not contribute to pressure gain because the flow is unconfined during heat release (i.e., it is reacting at near-constant constant pressure as in a conventional combustor). This is reflected in the performance results shown in Fig. 7, which trend opposite to those of Fig. 4. Here it is seen that the pressure gain of the 1-wave solution is substantially less than that of the 2-wave solution. The pressure gain of the 2-wave solution is slightly above that of the 3-wave solution. However, if the pressure gains are viewed relative to those from the Fig. 2 ideal simulations, the 2 and 3-wave solutions are shown to experience the same 9% performance reduction. The 1-wave solution shows a 19% reduction from the ideal. Considering the mass flux averaged reactant fractions above, this result implies that the amount of deflagrative pre-burning has a non-linear effect on performance. Pre-burning approximately 10% of the reactant reduces pressure gain by 9% from the ideal, while pre-burning 15% of the reactant reduces pressure gain by 19%.

As might be expected, mass flow rate is reduced when pre-burning is allowed since pre-burning reduces the density of the incoming reactant mixture. The detonation wave speed is barely affected by pre-burning.

1. *Contact Surface Deflagration*

Another region in the RDE flowfield where performance limiting deflagration can occur is along the contact surface between the incoming premixture and the post-detonative hot gas products. The portion of the white streamline above the dashed mixing delay line in Fig. 4 runs along this surface. In all the simulation results shown so-far however, there is virtually no deflagration occurring here. The mass flow rate across the plane labelled 1 in Fig. 3a is over 99% of the total flow entering the RDE inlet, and it has a mass flux averaged reactant fraction of z=0.99. This implies that virtually all of the reaction is detonative. This is an expected result because the deflagration requires both thermal and mass diffusion in order to take place, and the present simulations are all inviscid. Thus, the only diffusion that can occur is numerical. If the inlet was not an idealized one, and the simulation was in 3 dimensions (i.e. included radial variations), this contact surface would become significantly distorted [2]. This distortion, when combined with large pressure and azimuthal velocity gradients can lead to vorticity and an associated fluid 'tumbling' that effectively produces mass and thermal diffusion in the contact surface region, even if the simulation is inviscid. Real-world RDE's are therefore expected to have significant contact surface burning.

In order to cursorily examine this form of deflagration with the current simulation, the following axial diffusion terms are added to the energy and species components of the source vector, S in Eq. 5.

$$\underline{S} = \begin{bmatrix} 0 \\ 0 \\ \frac{p}{\gamma}\frac{dh}{dy} \\ 0 + D_T h \frac{\partial^2 T}{\partial T^2} + q_0 D_z h \frac{\partial^2 z}{\partial y^2} \\ -\rho z \begin{Bmatrix} K_0; T \geq T_{c0} \\ 0; T < T_{c0} \end{Bmatrix} h + D_z h \frac{\partial^2 z}{\partial y^2} \end{bmatrix} \tag{9}$$

The diffusion coefficients chosen are D_z=0.0014 and D_T=0.0075. These represent values that are approximately 500 times those associated with actual molecular diffusion. Although turbulent eddy viscosity could conceivably produce coefficients of these magnitudes, the present values are chosen simply because they are large enough to create a readily observable effect. For the same reason, the deflagrative reaction rate constant in Eq. 7 is raised to K_0=25, and the ignition temperature is lowered to T_{c0}=2.5.

Only the one-wave solution is considered, and the results are shown in the temperature contours of Fig. 8. The upper contour plot represents the solution with the diffusion coefficients set to zero (but with the modified K_0 and T_{c0}). The lower plot represents the solution with the diffusion coefficients set to the values listed above. The yellow streamline shown in each contour plot shows the path of the first particle of unreacted premixture to enter the RDE during the refill phase of the cycle. In the upper plot, this streamline follows the contact surface nearly exactly because there is no mechanism for deflagration to occur. In the lower plot, there is substantial deflagration which heats the flow in what is now a diffusion region. As a result, the axial velocity component increases and the streamline is further downstream (and with a much lower reactant mass fraction) by the time it intersects the oblique wave. The white

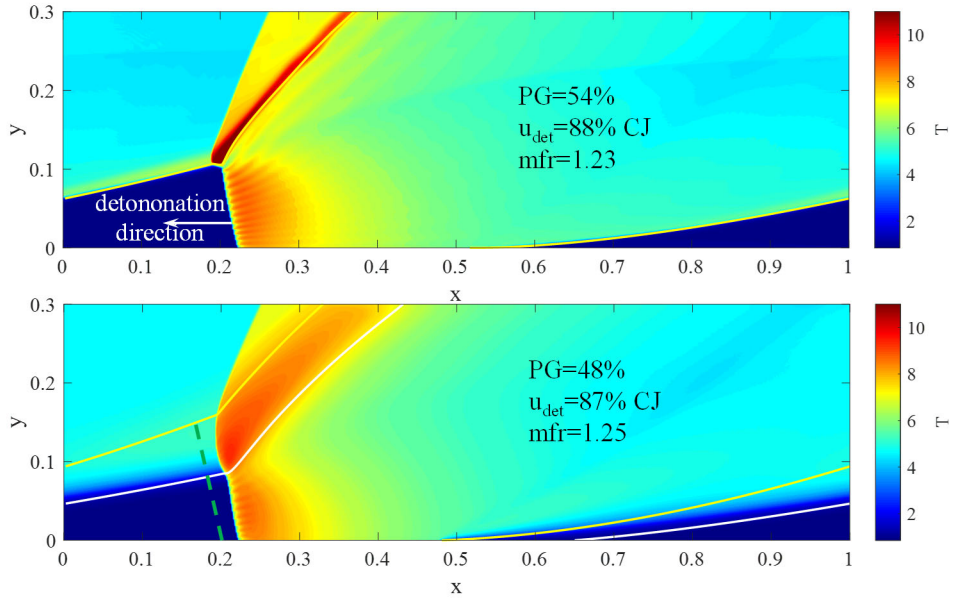

Fig. 8 Contours of temperature for the 1-wave solution with no diffusion (upper), and with diffusion (lower) controlling the contact surface deflagration

streamline in the lower plot follows the first particle of unreacted premixture to enter the RDE that passes through the detonation proper without undergoing any deflagrative reaction. The fluid in between these streamlines is, for the most part, deflagrating.

The mass flux averaged reactant fraction of the fluid crossing the dashed green plane in the lower contour plot of Fig. 8 is z=0.91. Thus, approximately 9% of the reactant is consumed in deflagration. This produces a pressure gain reduction of -6% when compared to the upper contour plot. The result indicates that contact surface deflagration incurs slightly less performance degradation per unit of reactant consumed than the deflagrative pre-burning examined previously. This may be because at least some of the contact surface burning may be reheating the fluid that has been through the detonation and is partially expanded (roughly akin to afterburning). While this is not an efficient way to add heat, it is not nearly as inefficient as adding heat prior to detonation. It is noted as well that even with very large diffusion coefficients (along with lowered T_{c0} and raised deflagration K_0), the one wave solution only deflagrated 9% of the reactant through contact surface deflagration. Deflagrative pre-burning, on the other hand, consumed 15% of the reactant for the one wave solution. These results indicate that contact surface burning is likely a secondary performance factor (compared to pre-burning) for the purposes of the present work. As such, no further simulations were conducted with the diffusion source terms of Eq. 8.

D. Impact of Combined Pre-burning and Mixing Delay

Given the opposing trends described in Sections B and C, it is interesting to consider the impact of combining them. This was done in the present work; however, the mixing delay was modified such that the same slow pre-burning deflagration (i.e., K_0=2.0) took place in this region rather than no reaction at all. This is an arguably more realistic approximation of the mixing delay. The results are shown in Fig. 9 in similar fashion to Fig. 2. It is shown that the impact on pressure gain is substantial for all three wave counts. Interestingly though, it is found that the 2-wave solution yields peak performance in terms of pressure gain. The additional reaction that takes place in the mixing delay region seems to be the greatest source of performance reduction. The mass flux averaged reactant fractions of the fluid entering the detonations are z=0.80, 0.84, and 0.84, respectively for 1, 2, and 3-wave solutions. Given this large pre-burning fraction, it is not surprising that the mass flow rate through this simulation scenario is the lowest of all those examined. It is also consistent with the results of Sections III B and C in that the detonation speeds listed in Fig. 9 are the lowest of all the simulation scenarios.

IV. Discussion

The performance results presented thus far are summarized in Fig. 10. The upper plot shows *PG* of the 1, 2, and 3-wave solutions for the Ideal, Mixing Delay, Pre-burning and Combined scenarios. The lower plot shows the *PG*

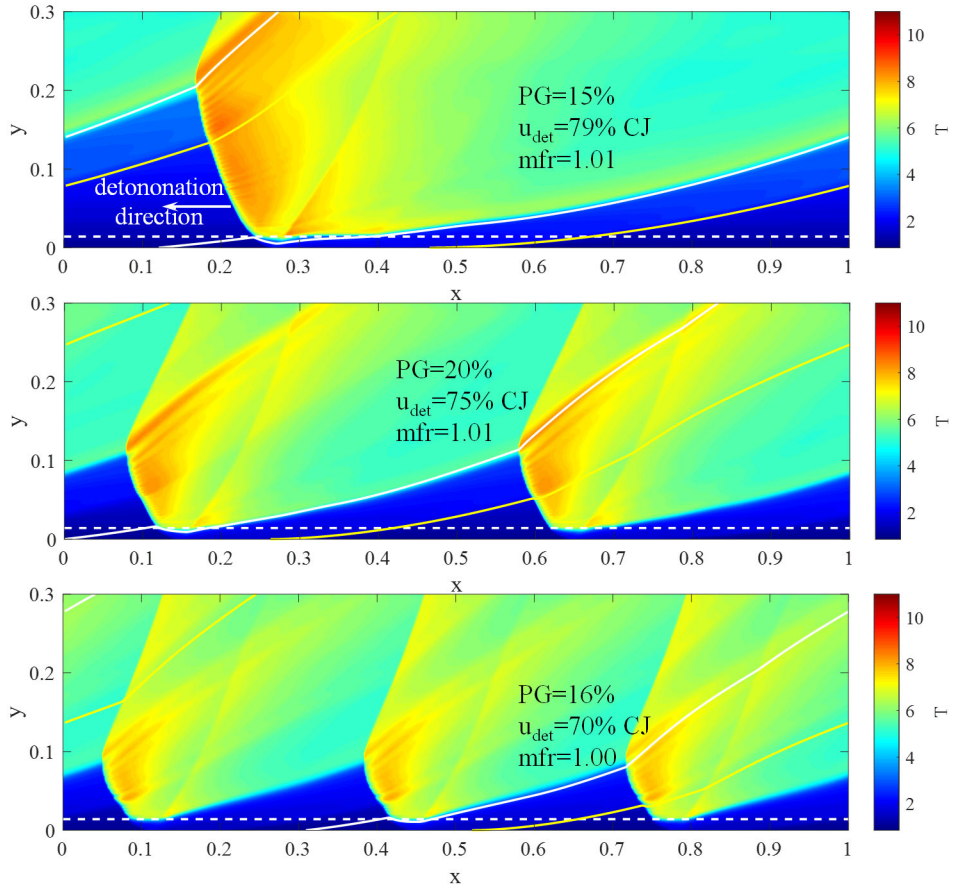

Fig. 9 Contours of temperature for the 1-wave (upper), 2-wave (center), and 3-wave (lower) solution to the RDE flowfield with mixing delay and deflagrative pre-burning

reduction from the Ideal scenario. The results highlight the challenges and criticality of RDE inlet design, along with shedding light on the performance impact of wave count. The inlet typically consists of a restriction followed by an abrupt expansion. This arrangement provides a surface against which the rotating detonation can generate thrust. It also mitigates backflow of hot, high-pressure, post-detonative fluid into the inlet manifold, and minimizes the dissipative upstream propagation of shock waves. However, the surface also becomes a kind of dump diffuser for fluid traveling in the forward direction during the refill process. This can lead to large momentum (i.e., total pressure) losses for the incoming flow. Successful inlet design must balance these two competing objectives of minimizing both backflow and forward flow losses [2]. The present results bring additional considerations to this already complex fluidic balance. Dump diffusers can act as flame holders by recirculating hot gas in the vicinity of the abrupt expansion. This can in turn lead to significant pre-burning and the noted performance degradation therefrom. Flame holding of this type is generally reduced if the fuel and oxidizer are not well mixed. As such, it is tempting to consider inlet fuel injection strategies that allow more mixing to take place in the RDE annulus proper. Doing so however, may generate the mixing delay losses just described. In summary then, the results indicate that developing high performing RDE's requires a multi-variable inlet design optimization strategy which successfully "threads the needle" of numerous competing factors.

On the other hand, the results shown thus far are largely qualitative. Neither the mixing delay length, nor the pre-burning rate constant choices were based on experimental measurements. Such measurements are exceptionally difficult to obtain with accuracy using current techniques. Thus, while the computed performance trends described in this study related to wave count, mixing delay, and pre-burning are likely correct, their degree of impact may require calibration.

A summary plot for *mfr* is shown in Fig. 11. Figure 11a is similar in format to Fig. 10a. There are no obvious trends in terms of wave count for various scenarios. Figure 11b combines data from Fig. 10a and 11a, and dispenses

with wave count as a parameter. Here, a clear correlation is visible. Higher *PG* tracks with higher *mfr*. Given that the mechanisms proposed for reduced *mfr* are directly related to *PG*, this correlation is expected. It is also somewhat intuitive. Nearly all air breathing propulsion systems demonstrate this trend.

Figure 12 summarizes the u_{det} data in the same manner as Fig. 11. Interestingly, Fig. 12a shows a clear trend in that u_{det} goes down with increasing wave count. However, Fig. 12b shows a poor correlation between *PG* and u_{det}.

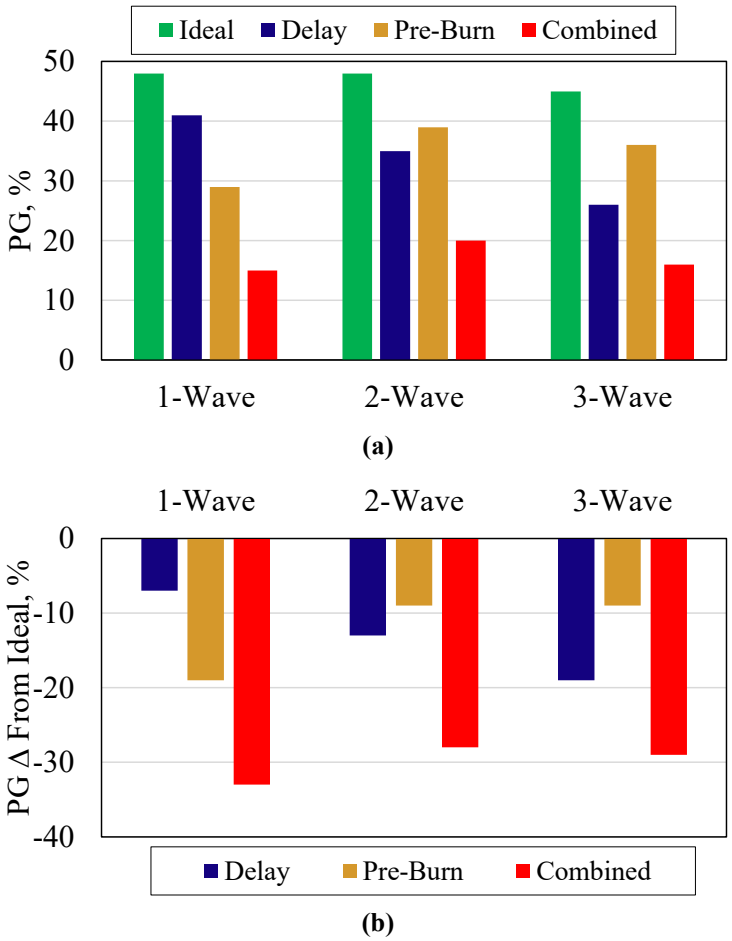

Fig. 10 Summary of (a) *PG* and (b) *PG* difference from the ideal simulation of the 1, 2, and 3-wave solutions for the Ideal, Mixing Delay, Pre-burning and Combined scenarios

V. Conclusion

A simplified two-dimensional computational fluid dynamic simulation was utilized to investigate the impact of the number azimuthally propagating waves on the performance of a Rotating Detonation Engine (RDE). The RDE was idealized in that it was assumed adiabatic, inviscid, and possessing a lossless inlet that does not allow backflow. To avoid complications arising from internal wave reflections the RDE configuration examined had no exit throat. The inlet was assumed lossless and did not allow backflow. One, two, and three wave solutions were computed subject to identical boundary conditions and grid resolution. For this fully idealized scenario the number of waves present has negligible impact on performance, though the detonation wave speed decreased as the wave count increased. Performance was measured as average total pressure gain across the device. The simple finite rate reaction mechanism of the simulation allowed user control over the relative amounts of deflagration and detonation that occur, as well as the presence and extent of a reaction delay associated with fuel and oxidizer mixing. With a mixing delay implemented, performance decreased as the number of waves increased. With increased deflagration prior to detonation, performance increased as the number of waves increased. With both effects simulated it was found that the two-wave solution performed better than either the one or three wave solutions. The causes for the performance trends were explored, and the implications for RDE inlet design were discussed. It was shown that for practical RDE's (i.e., those yielding positive pressure gain), the number of waves that were present impacted performance.

References

[1] Bach, E., et al, "Uncertainty Quantification of Kiel Probes for RDC Applications," AIAA-2021-0293, January, 2021.

[2] Paxson, D.E., Miki, K., "Computational Assessment of Inlet Backflow Effects on Rotating Detonation Engine Performance and Operability," AIAA-2022-1263, January, 2022.

[3] Paxson, D.E., "Numerical Analysis of a Rotating Detonation Engine in the Relative Reference Frame," AIAA-2014-0284, January, 2014, also NASA/TM—2014-216634.

[4] Kaemming, T.A., Paxson, D.E., "Determining the Pressure Gain of Pressure Gain Combustion," AIAA-2018-4567, July, 2018.

[5] Paxson, D.E., Fotia, M.L., Hoke, J.L., Schauer, F.R., "Comparison of Numerically Simulated and Experimentally Measured Performance of a Rotating Detonation Engine," AIAA-2015-1101, January, 2015.

[6] Paxson, D.E., Kaemming, T.A., "Influence of Unsteadiness on the Analysis of Pressure Gain Combustion Devices," *AIAA Journal of Propulsion and Power*, V. 30, No. 2, 2014, pp 377-383. DOI: 10.2514/1.B34913
[7] Paxson, D.E., "Examination of Wave Speed in Rotating Detonation Engines Using Simplified Computational Fluid Dynamics," AIAA-2018-1883, January, 2018.
[8] Schwer, D.A., Kailasanath, K., "Numerical Investigation of Rotating Detonation Engines," AIAA-2010-6880, July, 2010.
[9] Kaemming, T. A., Fotia, M. L, Hoke, J. L., Schauer, F. R., "Thermodynamic Modeling of a Rotating Detonation Engine Through a Reduced-Order Approach," *AIAA Journal of Propulsion and Power*, V. 33, No. 5, 2017 pp. 1170-1178. DOI: 10.2514/1.B36237
[10] Roy, A., et al, "Experimental Study of Rotating Detonation Combustor Performance under Preheat and Back Pressure Operation," AIAA-2017-1065, January 2017.
[11] Cho, K.Y., et al, "High-Repetition-Rate Chemiluminescence Imaging of a Rotating Detonation Engine," AIAA-2016-1648, January, 2016.
[12] Theuerkauf, S.W., et al, "Comparison of Simulated and Measured Instantaneous Heat Flux in a Rotating Detonation Engine," AIAA-2016-1200, January, 2016.
[13] Chacon, F., Gamba, M., "Study of Parasitic Combustion in an Optically Accessible Continuous Wave Rotating Detonation Engine," AIAA-2019-0473, January, 2019.
[14] Ayers, Z.M., Athmanathan, V., Meyer, T.R., Paxson, D.E., "Variably Premixed Rotating Detonation Engine for Evaluation of Detonation Cycle Dynamics," *AIAA Journal of Propulsion and Power*, accepted, publication pending, 2022.

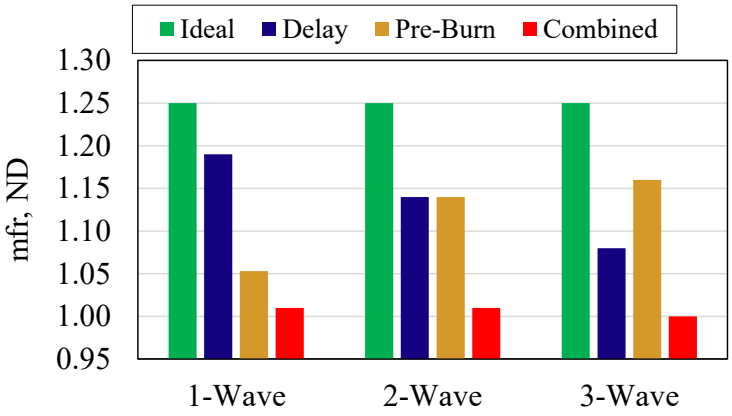

(a)

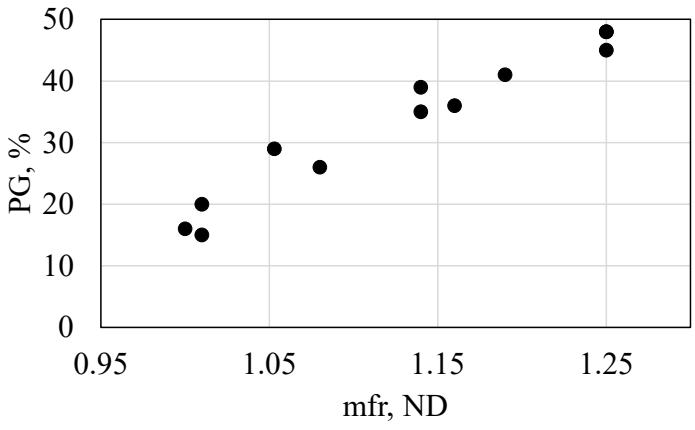

(b)

Fig. 11 Summary of (a) *mfr* of the 1, 2, and 3-wave solutions for the Ideal, Mixing Delay, Pre-burning and Combined scenarios; (b) *PG* vs. *mfr* for all solutions

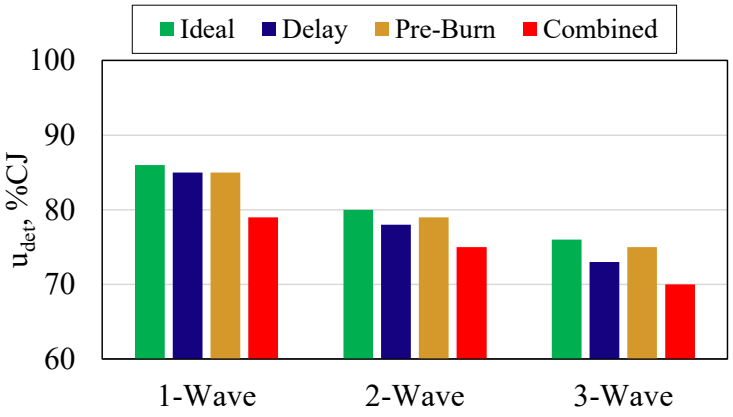

(a)

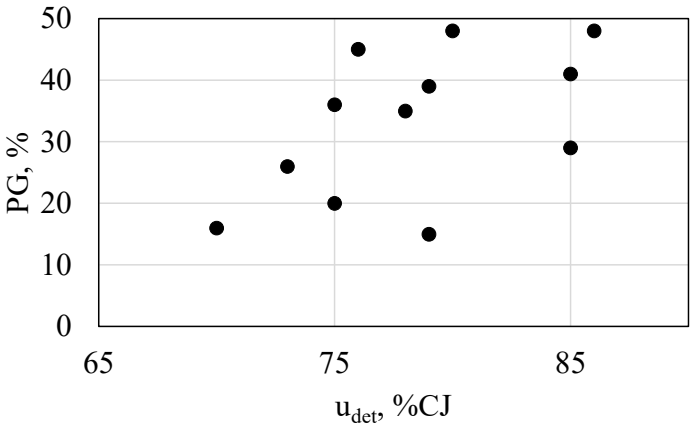

(b)

Fig. 12 Summary of (a) u_{det} of the 1, 2, and 3-wave solutions for the Ideal, Mixing Delay, Pre-burning and Combined scenarios; (b) *PG* vs. u_{det} for all solutions